Fault detection methods for 2D and 3D geomechanical numerical models

Anthony Adwan, Bertrand Maillot, Pauline Souloumiac, Christophe Barnes

Received: 27 July 2023 | Revised: 30 October 2023 | Accepted: 1 November 2023

DOI: 10.1002/nag.3652

RESEARCH ARTICLE

WILEY

Fault detection methods for 2D and 3D geomechanical numerical models

Anthony Adwan | **Bertrand Maillot** | **Pauline Souloumiac** | **Christophe Barnes**

CY Cergy Paris University, Maison Internationale de la Recherche (MIR), Neuville-sur-Oise, France

Correspondence
Anthony Adwan, CY Cergy Paris University, Maison Internationale de la Recherche (MIR), 1, rue Descartes, 95000 Neuville-sur-Oise, France.
Email: anthony.adwan@cyu.fr

Funding information
Federal Office of Topography swisstopo; Eidgenössisches Nuklearsicherheitsinspektorat; CY Cergy Paris Universite

Abstract

We develop automated methods for fault detection utilizing static stress and deformation fields at the onset of failure derived from numerical analysis. We calculate combinations and normalization of the distance from the Mohr circle to the Coulomb envelope, and of the second deviatoric strain invariant. A variation of the Cauchy distribution of these fields allows us to focus on the low values indicating rupture, with the help of the scale parameter δ. A threshold is then applied to decide at each spatial node of the mesh whether the material has reached failure or not. We then determine fault lines and planes from these isolated failure zones using image processing techniques, such as the Hough and the Radon transforms, or through a combined approach involving automated sorting of the nodes reaching failure through the k-means clustering technique followed by polynomial fitting to retrieve analytic expressions of the fault curves (in 2D) or fault surfaces (in 3D). The methods are efficient except when the stress field results in diffuse rupture zones that do not localize onto fault surfaces despite tuning δ. We also highlight the advantages of using the combined clustering/poly-fitting approach for 3D models compared to the image processing techniques. These automated fault detection methods should be useful in the interpretation of diverse failure mechanisms obtained through parametric sensitivity analyses requiring hundreds of simulations. The stress and strain fields used were derived from a numerical implementation of limit analysis, but classical finite-difference or finite-element techniques could have been used.

KEYWORDS

automated methods, fault detection, geomechanical models, numerical simulations, stress and deformation analysis, underground exploration

1 | INTRODUCTION

When rock experiences stress that surpasses its resistance, it undergoes rupture, a phenomenon that can occur due to a range of factors, including tectonic plate movements, volcanic activity, or human-induced activities such as mining, excavation, fluid injection, etc. Upon further loading, fractures coalesce into fault surfaces such that the rock on one side

of the fault shifts relative to the other side. Fault surfaces can be oriented vertically, horizontally, or obliquely at a specific angle, depending on the type and direction of the stress that caused the rupture.[1,2] Accurate detection and prediction of these fault planes are crucial for seismic and ground motion evaluations,[3–6] and geologic hazard assessment.[7,8]

With the recent advancements in computing technologies, whether applied in geotechnical engineering or earth science, numerical models have become indispensable for studying crustal and lithospheric deformations. These models have seen an increasing utilization in various areas, ranging from predicting the intricate behavior of complex structures and identifying potential instabilities in boreholes or caverns[9–12] to conducting fault analysis,[13] studying rock deformation and fracturing,[14] assessing groundwater resources, fluid pressure and analyzing fluid migration.[15,16]

In addition, be it for mineral mining[17–19] or simulation of geological evolution,[20–23] it is essential to accurately identify and incorporate faults into the model. But simulating geological growth and fault sliding are always considered a challenge for numerical applications due the discontinuous nature of the displacements, and to their dependency on both material weakening and the erosion/sedimentation process.[24–27] In general, numerical approaches can be divided into continuous and discontinuous methods. As their name suggests, continuous methods such as the Finite Element Method (FEM) are used to model materials that exhibit continuous behavior, while discontinuous methods such as Discrete Elements Methods (DEM) are used for fragmented behavior where interfaces and contacts are defined between the discrete elements. Both approaches have their own advantages and limitations, and the choice of the method depends on the specific application and the properties of the material being modeled.[28,29] For example, while Castro et al.[30] investigated fault-slip using 2D FEM and Hofmann and Scheepers[31] simulated fault slips by applying a cohesive strength change of the Mohr-Coulomb failure criterion using the continuous boundary element method (BEM), Garcia and Bray[32,33] showed that DEM analysis are suited for capturing the behavior of granular materials subjected to faulting.

In this paper, we are interested in developing a method that allows us to automatically detect faults when the material is at the onset of failure. For simplicity, we use stress and strain fields derived from the theory of limit analysis (LA).[34,35] LA aims to determine the maximum load that a structure can withstand before failure. The solution lies between an upper bound corresponding to an optimized virtual velocity field at failure (the kinematic approach) and a lower bound corresponding to an optimized balanced stress field that respects a failure criterion (the static approach). Since both strain and stress are determined independently by the respective approaches, there is no need for a stress-strain relationship. This means that, LA has the benefit of requiring less parameters than FEM or DEM to describe material behavior. Despite its simplicity, LA remains a highly robust approach that can handle complex geometries and loading conditions. Its use in the geological field was strongly highlighted by Maillot and Leroy[36] to assess the development of folds, then extended by Cubas et al.[37], verified by Souloumiac et al.[38] and later implemented in the SLAMTec software for sequential developments.[27,39] Afterwards, this same concept was adopted by Caër et al.[40] in a 2D parametric study over the Jura region.

Paper content is as follows: in the following section, we present the geological 2D and 3D models inspired from compressive fold-and-thrust structures and briefly present Limit Analysis before analyzing the stress and strain fields obtained from LA in order to detect incipient faults. This analysis involves the distance from the Mohr Circle to the Coulomb envelope and the second deviatoric strain invariant. They are combined, transformed and binarized to yield binary fields of ruptured/non ruptured states. The analysis continues with the detection of alignment (2D) or surfaces (3D) of broken points through image processing techniques (Hough and Radon transforms) and alternatively through clustering and polynomial fitting. Afterwards, we compare the results of fault detection using the different methods on each of the geological models and conclude on the general efficiency of the methods in 2D, and on the superiority of the clustering/polynomial fitting technique in complex 3D models.

2 | MODELING STRESS AND STRAIN FIELDS IN GEOLOGICAL MODELS

2.1 | Geological models

The geological prototypes adopted (Figure 1) represent the frontal part of an accretionary wedge with a 3° dipping topographic slope, leading to a decrease in thickness from 3.71 km at the back to 2.5 km at the front of the relief which is prolonged by a flat layer. They extend 32.5 km in length and are formed by Coulomb materials (Table 1). The specific density for all materials is set to 25.5 kN/m^2.

Mechanically speaking, these reliefs are explained by the critical Coulomb wedge (CCW) theory,[41] where the wedge shape results from the balance between the strength of the wedge material, considered as a uniform Coulomb material, and the basal friction angle.[42,43] In 2D, the above described geometry is divided into a single layer model made of material A (Figure 1A) and a multiple layer model with materials A and B, the latter being weaker (Figure 1B). The bulk material

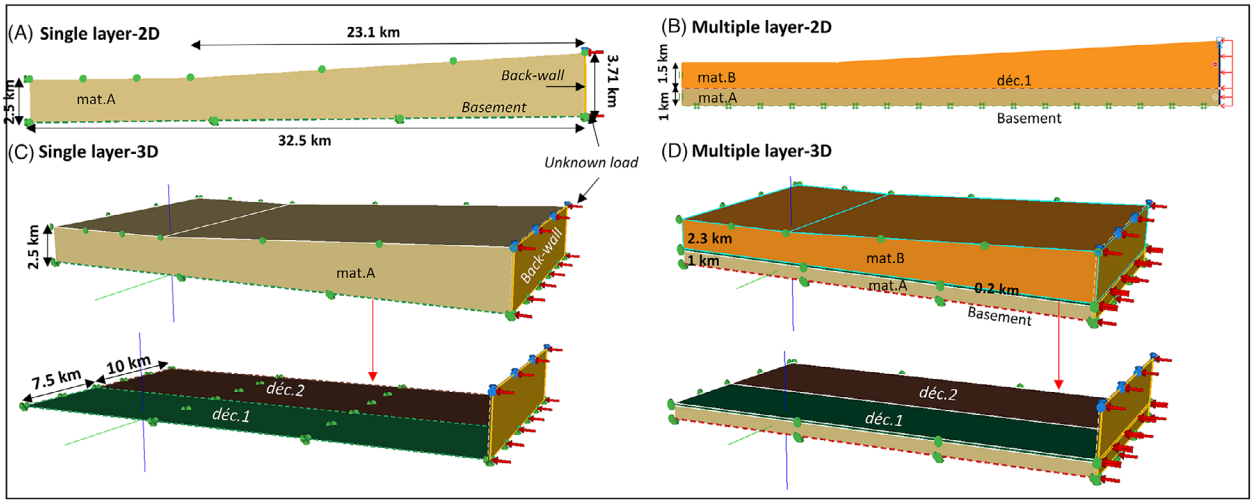

FIGURE 1 Models overview. (A) 2D model representing an accretionary wedge with a length of 32.5 km. It is formed by a single layer Coulomb material(mat.A) overlaying a basement. At the back-wall, an unknown load is applied as shown by the red arrows. (B) The model is divided into two layers (mat.A and mat.B) separated by an upper décollement level (déc.1). (C) The model is extended into 3D with a width of 17.5 km overlaying a heterogeneous double décollement (déc.1 and déc.2). While in (D), the model is transformed into a multiple layer model also formed by mat.A and mat.B separated by a 200 m thick heterogeneous décollement level. At the back-wall a rigid plate is defined and represented in yellow while the plates BC are represented in blue.

TABLE 1 Table presenting the properties of the materials used in the numerical applications.

	Friction angle (°)	Cohesion (MPa)	Specific density (kN/m^2)
Material A (mat.A)	$\phi_{\text{mat.A}} = 30$	$c_{\text{mat.A}} = 1$	25.5
Material B (mat.B)	$\phi_{\text{mat.B}} = 20$	$c_{\text{mat.B}} = 1$	25.5
Basement	$5 \leq \phi_{\text{basement}} \leq 10$	0	25.5
Décollement 1[a] (déc.1)	$3 \leq \phi_{\text{déc.1}} \leq 20$	0	25.5
Décollement 2[b] (déc.2)	$5 \leq \phi_{\text{déc.2}} \leq 22$	0	25.5

[a]Only for the 3D models and the 2D multiple layers.
[b]Only for the 3D models.

in both cases overlay a rigid basement with a cohesionless surface and a varying friction angle. The 3D simulations also involve a single layer model (Figure 1C) and a multiple layer model (Figure 1D). The single layer model is merely a lateral prolongation of the 2D single layer model. It extends 17.5 km in width and overlays a rigid basement divided into two distinct parts (déc.1 and déc.2) respectively spreading laterally over 7.5 and 10 km with potentially different friction angles and without cohesion. The multiple layer 3D model is formed by an upper material B layer with a minimum thickness of 2.3 km, separated from the 1 km thick material A layer by a 200 m thick heterogeneous cohesionless décollement. Material A rests on a homogeneous rigid basement with friction angle $\phi_{basement}$ and no cohesion.

2.2 | Practical implementation of limit analysis

Determining collapse loads in soil mechanics, requires the assumption that the materials exhibit a rigid, perfectly plastic behavior. Yet, some analytic methods used to solve stability problems such as Fellenius circles do not verify the governing mechanical equations. LA helps explain this discrepancy and offers a foundation for rational methods that lead to precise solutions for these problems.[44] By considering perfectly plastic solids, LA does not require any elastic parameter and only follows the principal of maximal work and the convex yield criterion chosen. In this paper, we adopt the calculation algorithm of the commercial software OPTUM G2-G3[45] and we use Coulomb materials, so that LA follows the Mohr-Coulomb criterion. We define the boundary conditions as follow:

- Normal supports (i.e., blocking any movement normal to the edges) on both west and east edges of the 3D models (assuming that North is the compression direction).

- Normal supports at the front (northern) wall.
- Fixed support (i.e., blocking any normal or tangential movements) at the base of the model.
- Defining basements and 2D décollements as shear planes having the appropriate Coulomb parameters. This feature is used to model internal discontinuities and to define interfaces between different solid layers.
- Constructing the back-wall with a rigid plate supported by two plate BCs (feature in OPTUM G2 and G3 similar to a hinge). This allows us to restrict unwanted displacements and rotations. On the intersection surface between the plate and the bulk materials, we also consider an interface having the same frictional properties as the bulk material in contact.
- Defining a distributed unknown compressive load α*1 kN/m^2. α being the load multiplier.

LA aims to understand how structures behave when they are solicited up to their mechanical resistance. It consists of two independent so called upper and lower bound analyses (also called "kinematic" and "static" approaches, or "external" and "internal" approaches). The lower bound is the maximum force that the structure can withstand without permanent deformation. It is obtained by optimizing the stress field in the structure so that its integral on the back-wall is maximum. Of course the stress field must be in mechanical equilibrium and must verify the Coulomb criterion. On the other hand, the upper bound is the minimum force that can cause permanent deformation in the structure. It is obtained by optimizing a virtual velocity field and calculating the associated force using the maximum strength theorem (e.g., ref. [36]). For 2D models we follow these approaches and we perform separate calculations for both bounds. However, for 3D models we adopt a more efficient optimization procedure following the mixed principles.[46–48] Rather than calculating precise bounds, these principles consider both stress and velocities as primary variables and offer compromise solutions that are often closer to the exact solution than the upper and lower bounds.

In order to balance time and precision, we adopt uniform meshing with a 40,000 tetrahedron discretization for 3D models and 10,000 triangular meshing for 2D models. The calculation method is element-based, which means that a distinction is made between stress nodes and geometric nodes, although they have the same coordinates. Stress nodes are specific nodes associated with each discretized element, making them unique on an element-wise basis. As a result, a geometric node has as many stress values as the number of surrounding elements. Final stress values at geometric nodes are derived by averaging the values of stress nodes with the same coordinates weighted by the surface (or volume in 3D) of the element to which they belong. There are two possibilities for reassembling the results obtained over the final geometric nodes. First, taking into consideration independent domains defined following the geometric and structure features of the model. Second doing a full reassembly and thus averaging the values obtained even through the discontinuous features. It is true that the first assembly is highly advantageous for fault analysis since it allows the construction of discontinuous stress and strain fields. But, the models studied in this paper do not present inherent faults thus we adopted the second reassembly procedure.

3 | RUPTURE DETECTION

3.1 | Distance to the Coulomb failure criterion

Let c be the cohesion of a frictional Coulomb material and ϕ its friction angle. The aim is to calculate the value of the distance d between a generic Mohr circle and the Coulomb failure envelope (Figure 2A). From simple trigonometry,

$$sin(\phi) = \frac{d + R}{D} \tag{1}$$

where the radius of the Mohr circle is

$$R = \frac{|\sigma_1 - \sigma_3|}{2}, \tag{2}$$

and

$$D = \frac{|\sigma_1 + \sigma_3|}{2} + \frac{c}{tan(\phi)}, \tag{3}$$

therefore

$$d = \frac{|\sigma_1 + \sigma_3|}{2} sin(\phi) + c * cos(\phi) - \frac{|\sigma_1 - \sigma_3|}{2}. \tag{4}$$

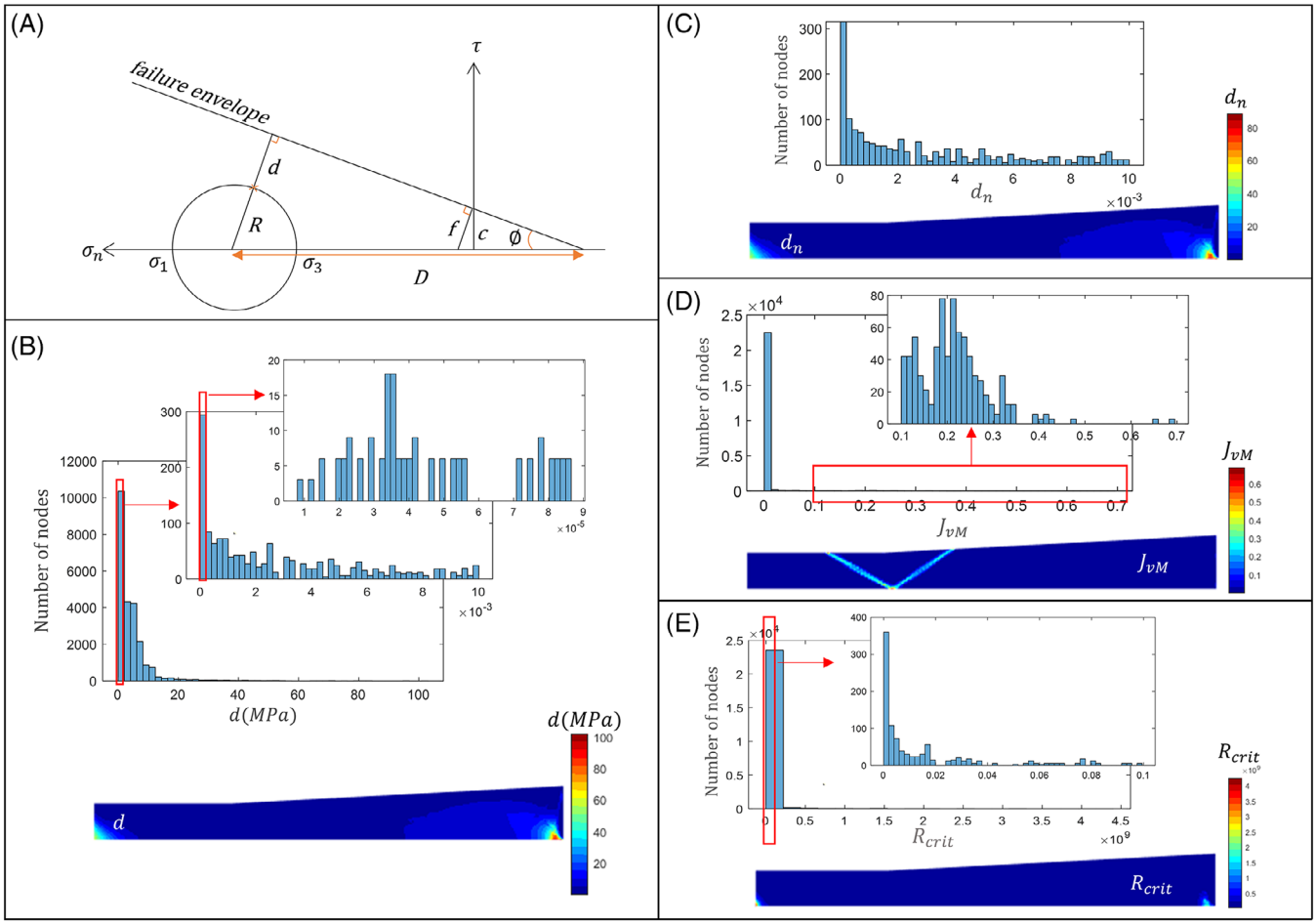

FIGURE 2 Example of a 2D single layer model with a $\phi_{basement}$ of 5°. (A) Representation of the Mohr-Coulomb diagram: σ_1 and σ_3 are the two extreme principal stresses, d is the distance between the Mohr circle and the envelope also considered as the yield criterion. f is the material related dimension used in the calculation of d_n. (B) Presents the histograms showing the variations of d over the stress nodes with a focus on the values lower than 0.01 and 10^{-4}. (C) d_n representation is shown with the histogram re-partition of the nodal values lower than 0.01. (D) Representation of the J_{vM} values obtained with histograms showing the variation of these values over all the stress nodes and a focus on the values higher that 0.1 while in (E), the histograms show the value of R_{crit} with a focus on the values smaller than 0.1. For the representations, the color-bars show the high values of the variables in red while the low values are in dark blue.

Since we are using the geotechnical software OPTUM CE, the engineering convention consider negative stress values for a compression regime (as in Figure 2A), but the definition (4) is valid regardless of the sign convention.

Wherever d is equal to zero, the linearly assumed failure envelope is tangent to the Mohr-Coulomb circle and the given node attains rupture. However, the stress field determined by LA may only rigorously reach failure on a very small number of nodes that would be insufficient to determine a full fault surface. This suggests the need to determine a rupture threshold, that is a value of d below which the nodes are considered as ruptured. Before determining this threshold, let us examine the simple example of the single layer 2D model with a basement friction angle of 5°. Figure 2B, shows the distribution of the d values obtained over all the stress nodes (there are more than 25,000 stress nodes for the 10,000 triangular elements). At first glance, the majority of the nodes (10,200) have values between 0 and 2 MPa highlighting a high concentration towards the lower values. Consequently, simply choosing low values as being close to zero is an invalid assumption. By focusing on the values of d lower than 0.01 MPa, the number of stress nodes drastically decreases to 1,439. In the last histogram, only three nodes have d values less than 10^{-5} MPa. It becomes evident that in order to perform fault extraction, three stress nodes are insufficient and thus it is essential to define a personalized rupture threshold allowing the determination of a zone portraying an incipient fault.

More generally, for heterogeneous models for example, differences in the material strengths may lead to strong stress field variations, and a single threshold value may not be sufficient to detect ruptures in all regions. For this reason, we

propose a value normalized by the local material resistance defined as a combination of the Coulomb parameters that is graphically similar to d (Figure 2A):

$$f = \frac{c}{cos(\phi)}, \tag{5}$$

so that

$$d_n = \frac{d}{f}. \tag{6}$$

By adopting d_n we measure the distance to rupture relatively to the material strength (Figure 2C). Of course, the yield tendencies are not affected by this normalization, in this example, because the material is uniform. Note that the material cannot be considered cohesionless with this choice of normalization (if $c = 0$ then d_n tends to infinity). This is coherent with the existence of a free surface in our geological models: to avoid rupture at the surface we must give some cohesion to the materials.

3.2 | Second strain invariant

Understanding failure in rock mechanics also implies characterizing the displacement of every point constituting a rock mass when subjected to specified boundary conditions.[49] Since we are interested in fault detection, that is rupture involving shear of the material, we calculate the second invariant of the deviatoric part $\underline{\underline{\tilde{\varepsilon}}}$ of the strain tensor as follows:

$$\begin{aligned} J_2 &= \frac{1}{2}(trace(\underline{\underline{\tilde{\varepsilon}}}^2) - trace(\underline{\underline{\tilde{\varepsilon}}})^2) \\ &= \frac{1}{6}[(\tilde{\varepsilon}_{xx} - \tilde{\varepsilon}_{yy})^2 + (\tilde{\varepsilon}_{xx} - \tilde{\varepsilon}_{zz})^2 + (\tilde{\varepsilon}_{yy} - \tilde{\varepsilon}_{zz})^2] + \tilde{\varepsilon}_{xy}^2 + \tilde{\varepsilon}_{yz}^2 + \tilde{\varepsilon}_{xz}^2. \end{aligned} \tag{7}$$

Although not necessary, here we express J_2 following an equivalent form of the von Mises stress[50] but for strains, henceforth named von Mises strain (J_{vM}), which can be expressed as:

$$J_{vM} = \sqrt{3J_2} \tag{8}$$

Some of the common failure criteria based on strains resolve around defining an ultimate allowable strain level above which the model is considered to have failed. Typically, this limit is determined through experimental testing and theoretical models.[51–54]

Analysis of Figure 2D indicates that values of J_{vM} greater than 0.1 represent failure zones corresponding to the development of conjugate reverse faults. While this observation is expected for LA, where virtual stress and strains are optimized at the onset of rupture, it is not valid for general FEM or DEM simulations. In fact, it is true that a high J_{vM} indicates that a material is under a significant amount of stress, leading to higher deformation, but it does not necessarily imply that rupture has occurred unless it is higher than some predefined critical strain value.

3.3 | Ratio of distance to strain

We also propose the use of the ratio:

$$R_{crit} = \frac{d_n}{J_{vM}} \tag{9}$$

that provides a more general criterion accounting for both the deformation and the material strength properties while respecting the same tendencies as d_n (Figure 2E). In the following sections, we present the methodology for evaluating failure using these three different criteria: d_n, J_{vM}, and R_{crit}.

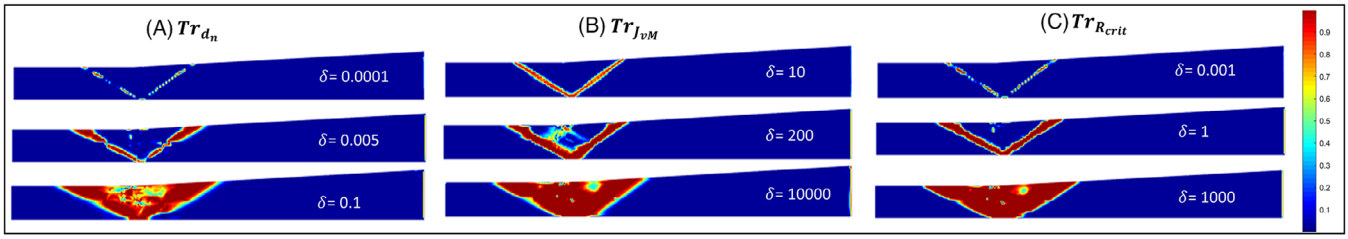

FIGURE 3 Effect of the scale parameter δ used in the Cauchy mathematical transformation of all three criteria: (A) d_n, (B) J_{vM}, and (C) R_{crit}. An extreme value of delta, too high or too low, leads to either very thin or very large rupture zones. The color bar used in these representation shows the high values of each transformation in red, while the low values are in dark blue.

3.4 | Mathematical transformation and binarization

Following what was previously presented, we need to focus on the low, positive values of d_n, R_{crit}, and $1/J_{vM}$. In order to do so, we apply a variation of the probability density function (PDF) of the Cauchy distribution.[55] While the initial equation is:

$$F(x) = \frac{1}{\pi\delta}\frac{\delta^2}{(x-x_0)^2+\delta^2}, \tag{10}$$

the simplified variation adopted in this paper is given as follows:

$$C(x) = \frac{\delta^2}{(x-x_0)^2+\delta^2}, \tag{11}$$

where x is the random variable, x_0 is the location parameter (representing the median of the distribution), and δ is the scale parameter. A larger value of δ leads to a wider distribution, while a smaller value of δ leads to a narrower distribution. The scaled version of this distribution (Equation 11) is generally used in signal and image processing. It maintains the symmetry around x_0 but is not normalized to a have a total area of one under the representing Gaussian curve. Taking $x_0 = 0$, and dividing by δ^2 the simplified Cauchy distribution becomes:

$$C(x) = \frac{1}{1+\left(\frac{x}{\delta}\right)^2} \tag{12}$$

and by applying this form over our criteria, their transformed forms are written as:

$$Tr_{d_n} = \frac{1}{1+\left(\frac{d_n}{\delta}\right)^2} \tag{13}$$

$$Tr_{R_{crit}} = \frac{1}{1+\left(\frac{R_{crit}}{\delta}\right)^2} \tag{14}$$

and

$$Tr_{J_{vM}} = \frac{1}{1+\left(\frac{1}{J_{vM}*\delta}\right)^2} \tag{15}$$

in this case, δ represents the rupture scale coefficient responsible for adequately determining a rupture zone. Figure 3 shows the above three transforms of the same single layer 2D model for different values of δ. For Tr_{d_n}, $Tr_{J_{vM}}$, and $Tr_{R_{crit}}$ if δ is set to a very small value (respectively 10^{-4}, 10, and 10^{-3}), the detected rupture zone is thin and discontinuous (for

Tr_{d_n} and $Tr_{R_{crit}}$) since fewer nodes are considered at rupture. Conversely, a large δ leads to a wider failure zone, as shown for $\delta = 0.1$, 10,000 and 1,000 respectively. It is worth noting that the representation obtained using $Tr_{R_{crit}}$ is smoother and clearer than both Tr_{d_n} and $Tr_{J_{vM}}$ since it fuses both representations (for comparison purpose, δ used for $Tr_{R_{crit}}$ is taken as equal to the multiplication of the respective δ values used for Tr_{d_n} and $Tr_{J_{vM}}$).

The next step is to decide, for each node, whether it has reached failure or not: we call this binarization. In order to better compare the various numerical outcomes, we first redistribute the computed criterion values across a predefined regular grid using natural interpolation based on Voronoi tessellation.[56] The choice of the grid is arbitrary and has no direct effect on the detection process. In this paper, to simplify the process we decide to consider a grid with a scale close to the initial model dimensions and so we chose a grid of 1000×100. The values obtained through equation 12 vary between zero and one. For a chosen δ, the higher the value of x, the closer the transform is to zero. Our aim is to focus on the low values of x implying the focus on the high values of the transformed criteria, thus the values closer to one. Therefore, after several essays to prevent excessive filtering, we consider that each node has reached failure if its criterion value (Tr_{d_n}, $Tr_{J_{vM}}$, or $Tr_{R_{crit}}$) is higher than 0.7 of its maximum value in the grid. Following this choice the rupture condition can be expressed as follows:

$$\frac{1}{1+\left(\frac{x}{\delta}\right)^2} \geq 0.7 \frac{1}{1+\left(\frac{x_{min}}{\delta}\right)^2} \tag{16}$$

and since x_{min} tends to zero:

$$\delta \geq \sqrt{\frac{7}{3}} x. \tag{17}$$

For a chosen criterion threshold (x), we calculate a corresponding δ. Any criterion value that satisfies the condition given by Equation 17 for this δ is considered to be at rupture. Conversely, by selecting a specific δ, we can derive the criterion values that are considered at rupture without the need to define an initial threshold. As an example, when studying $Tr_{R_{crit}}$ with δ values of 0.001, 1, and 1000, as shown in Figure 3, the corresponding R_{crit} values considered at rupture are smaller than 0.00065, 0.65, and 654, respectively. These values align with the observed tendencies in the histograms presented in Figure 2E. To illustrate the results of binarization on a regular grid obtained for $Tr_{R_{crit}}$ in the same 2D example under a δ value of one, refer to Figure 4A.

4 | FAULT DETECTION

Once the rupture zones are cast as a binary field on a regular grid, various methods can be employed to extract fault curves in 2D or fault surfaces in 3D. We introduce three methods drawn from the fields of image processing and mathematical poly-fitting using examples in 2D. Through these techniques, we can delineate fault geometries and determine the best fitting analytic expressions.

4.1 | Hough transform

Detecting simple shapes such as straight lines is a basic goal of image processing. One of the common methods is the Hough transform. The original aim of Hough's patent[57] was the same as ours here: to detect alignments of points in binary images. The idea behind this method is that the equation of a straight line $y = ax + b$ can also be written as $b = -xa + y$. Consequently, points which are colinear in the image space intersect at a same point P(a,b) in the parameter space and vice versa.[58] In this article the Hough line detection algorithm adopted converts the binary image from the Cartesian coordinate system (Figure 4B1) to a Hough domain using the parameters (θ, ρ) proposed by Duda and Hart.[59] The line equation becomes:

$$\rho = cos(\theta)\, x + sin(\theta)\, y \tag{18}$$

where $|\rho|$ is the distance from the line to the origin, considered at the top left side of the image (Figure 4B2). The parameter space is divided into a uniform grid, following the precision required for the parameter estimation, and each grid cell

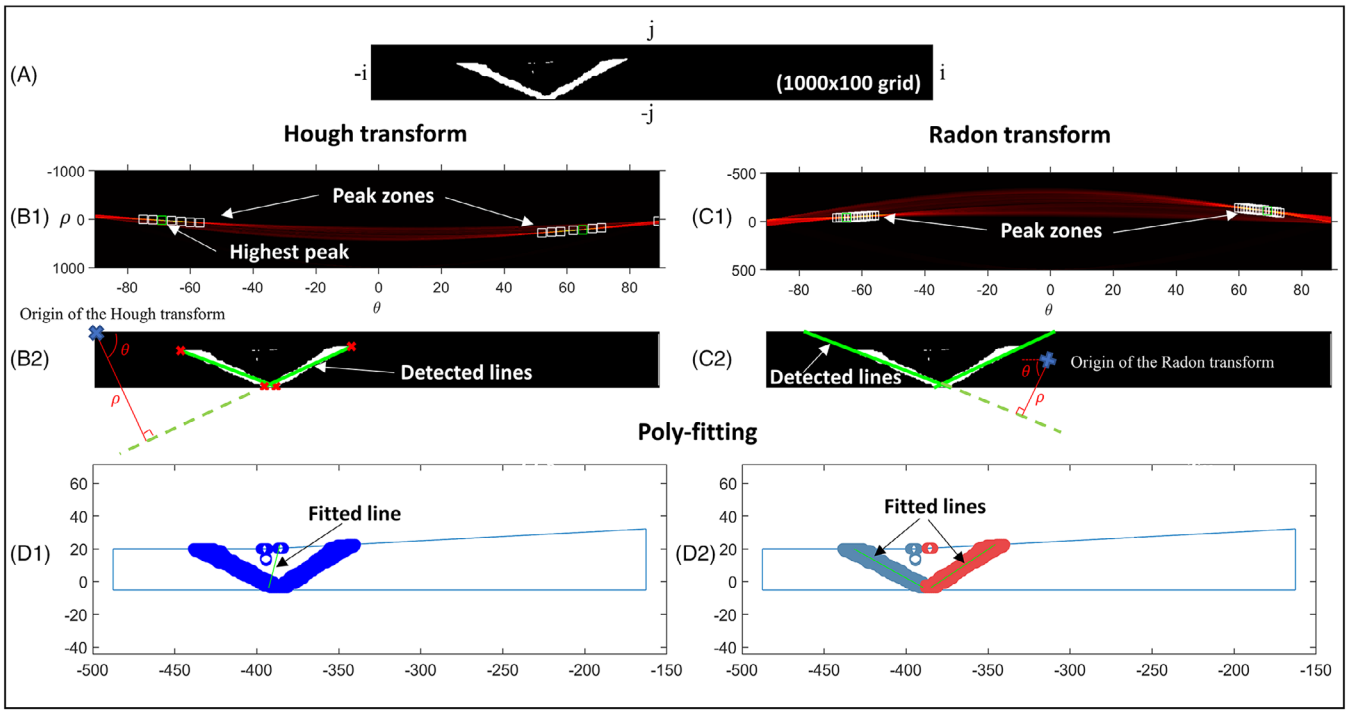

FIGURE 4 Results obtained from applying all three line detection algorithms (Hough (B), Radon (C) and Poly-fitting (D)) over the single layer example under the $Tr_{R_{crit}}$ criterion. The detection is applied over a 1000×100 binarized grid where the rupture zone is represented in white (A). The intersection of different sinusoidal curves in the Hough (B1) or Radon domain (C1) yield peak zones in which the highest value represents a line in the initial image (B2,C2). The origin of the Hough transform is at the top left of the image (B2) while the origin of the Radon transform is located at the middle of the image (C2). θ and ρ are the line parameter used in the Hesse normal line equation form. The detected lines are represented in green and the segmentation limit for the Hough transform is marked in small red crosses. For the poly-fitting method, the nodes verifying ruptures are represented in small blue voided circles. The first fitting attempt is shown in D1 while D2 shows the final lines obtained after clustering. The two distinct clusters are represented in blue and red.

contains a counter. For each white pixel in the initial image (i.e., a point that has reached rupture), we identify all grid cells (θ, ρ) corresponding to a line passing through that pixel, and we increment their counter by one. Therefore, colinear white pixels of the image correspond to grid cells of the parameter space with higher counters (see Peak zones, Figure 4B1). The corresponding parameters (θ, ρ) of each local maximum represent alignments of white pixels in the image that we interpret as faults (the green lines in Figure 4B2).

The steps explained previously are valid for 2D image processing. The extension to plane detection in 3D is straightforward.[60] However, we expect that fault surfaces in 3D are more curved than fault lines in 2D implying that "plane-stitching" may be necessary. In addition, the 3D Hough transform is computationally inefficient and it is highly dependent on the mesh precision. Consequently, extending the algorithm to 3D is not efficient in our case. Nonetheless, we present an alternative 2.5D approach that involves line-detection over a series of cross-sections, leading to the definition of a 3D fault surface.

4.2 | Radon transform

The Radon transform[61] is a mathematical technique that transforms an image or a 3D block of data into a set of line integrals in a projection domain. This technique is commonly used in medical imaging, specially in computed tomography (CT) scans. In seismic applications, this method is also adapted for hyperbola detection in seismograms. It is more general than the Hough transform as it can be applied to images with real values and not only binary, although we use it here on binary images. We use the same parametrization (ρ, θ) for the lines, but this time with the origin located at the center of the image (Figure 4C2). The image is considered as a function f(x,y) defined over $x \in [-i, i]$ and $y \in [-j, j]$ (Figure 4A).

The Radon transform is written as[62]:

$$R(\rho,\theta) = \int_{-i}^{i}\int_{-j}^{j} f(x,y)\delta_D(xcos\theta + ysin\theta - \rho)dxdy \tag{19}$$

where $R(\rho,\theta)$ is the Radon transform of f(x,y) and δ_D is the Dirac delta function. By applying this to the binary image of Figure 4A, we obtain the Radon transform of Figure 4C1. Just like in the Hough space, we can detect peak zones with a peak-finding algorithm. Each peak represents a line detected in the initial image (green lines in Figure 4C2). Finally, we note that for the same reasons stated above, we will not be extending this approach to full 3D since it can also be used in a 2.5D implementation just like the Hough transform. Note that since we are considering the highest peak, the resultant line may present a small slope error compared to the original fault dip angle (Figure 4C2).

The Hough transform and the Radon transform look similar, yet they are different methods. By accumulating votes for potential lines through a binning process, the Hough transform identifies lines in a binary image while the Radon transform operates on images with continuous real values and calculates all possible line integrals generating a Radon projection that is reversible. The output of both these methods can be subjected to post treatment in order to obtain line segments depending on the purpose of the study. Since the Hough transform is frequently used with binary images, straightforward algorithms exist, enabling segmentation by checking the edges of the white pixels forming the detected lines.

4.3 | Polynomial fitting

We also opt to use polynomial fitting to approximate a curve function that fits the failure data cloud. The degree of the polynomial controls the number of curves that can be determined by the defined equation. For instance, a first degree polynomial represents a plane, while a third degree polynomial can have two curves. When applying this technique to geological data, several verification steps are necessary before obtaining the final result. The example of Figure 4 contains two conjugate reverse faults, as visible in its binary version. Since they appear rather linear, we use first degree polynomials to fit the distribution of ruptured nodes in Figure 4D1. However, the challenge is to determine automatically the number of faults to be fitted. To separate the white pixels in clusters that correspond to individual faults, we employ the well-known k-means algorithm[63] along with the Davies-Bouldin index.[64] By doing so we are considering both the inter-cluster similarity and the intra-cluster dissimilarity to automatically choose the adequate number of clusters. The steps are as follows:

1- A fitting with a linear polynomial is calculated over all the white (or broken) pixels, using the polynomial fitting function developed by D'Errico.[65]
2- If the regression coefficient R^2 is below 80%, a clustering step is applied to divide the data into several clusters over which polynomial fitting is performed (Figure 4D2).
3- A secondary R^2 check is applied on each obtained cluster following the same 80% regression coefficient in order to obtain the best fit possible.
4- If the secondary R^2 check is not verified, each cluster is then divided into-sub-clusters over which polynomial fitting is applied.

5 | APPLICATION TO COMPLEX GEOLOGICAL MODELS

5.1 | Multiple layer 2D

In this section, we assessed the applicability of our approach to a double-layered 2D model, where $\phi_{basement}$ was set to 10° and $\phi_{déc.1}$ to 5° (Figure 1B). We observe that déc.1 is activated and a pop-up (fault/back-thrust) system appears clearly at the end of the surface slope in mat.B. This means that the wedge formed of mat.B above déc.1 is stable in the sense of the CCW theory.[42] The bottom layer made of mat.A, being more resistant, but lying on a basement with higher frictional strength than déc.1, undergoes large deformations near the back-wall but with rather dispersed failure zones that are transferred in mat.B layer where they generate a pop-up V-shaped structure of diffuse deformations nearing rupture (Figure 5A).

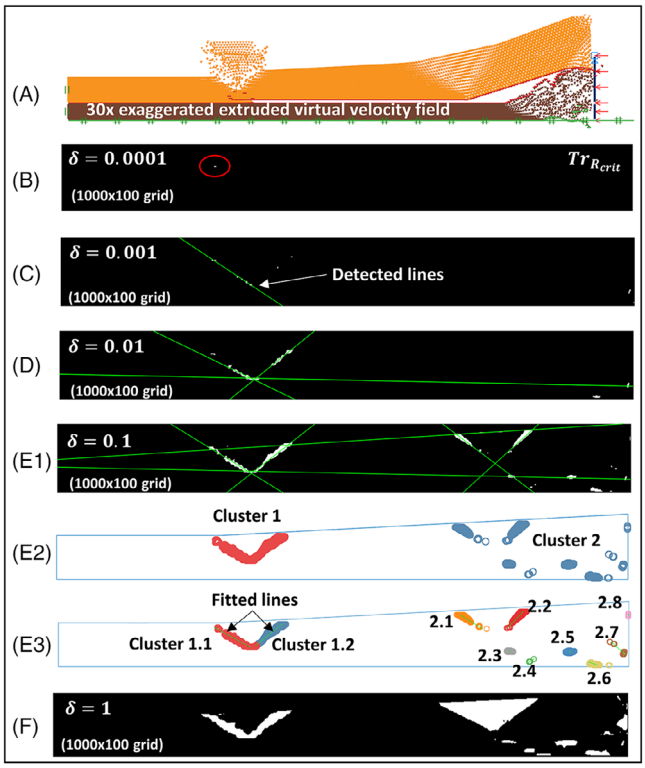

FIGURE 5 Results obtained from applying the Radon transform and polynomial fitting to the 2D multiple layer model (Figure 1B). (A) shows a 30 times exaggerated extruded velocity field. The 1000 × 100 binarized grid obtained for $Tr_{R_{crit}}$ with a δ value of 0.0001 is given in (B). The single node attaining rupture is in white and highlighted with a red circle. In (C), (D) and (E1) the results obtained from applying the Radon transform are shown respectively for δ values 0.001, 0.01 and 0.1. The detected lines are colored in green. (E2) shows the two main clusters obtained after the first fitting attempt, while (E3) presents the final sub-clusters with their respective fitting results. Lastly, in (F), the binarized grid under a $\delta = 1$ displays large and dispersed rupture zones depicted in white.

Following the same process as previously described, we tested the Radon and the poly-fitting criteria since both Hough and Radon yield similar results. To do so, we first had to choose an adequate δ. But, we remind that our objective is to automate fault detection, so manually checking our criterion values each time to define δ is not a valid option. This is why we suggest the following procedure. The detection algorithm starts with a low value of δ and tries to extract a fault. In the eventuality that this process is not possible, δ is augmented and extraction is reattempted. We applied this approach over the double-layered 2D model. Starting with a $\delta = 10^{-4}$ a single ruptured node was detected and fault extraction was impossible (Figure 5B). We then defined a δ factor of 10 for each iteration. The second attempt was able to detect a single line representing the reverse fault created at the end of the surface slope (Figure 5C). If our goal was to simply detect the dominant fault curve, we could have stopped the algorithm at this step. But here, the intention is to present the full fault detection approach while testing its limits so we continued the iterations. For $\delta = 0.01$, the frontal pop-up was adequately detected in addition to a line indicating the start of the rupture zone in mat.A near the back-wall (Figure 5D). The case with a $\delta = 0.1$ clearly shows the creation of two pop-ups, one at the front and one at the back in mat.B. In addition, two other lines were also detected, one following the slope surface and the other signaling the rupture in mat.A (Figure 5E1). The algorithms used in this paper follow the general line detection steps, thus no prior knowledge is implemented in order to eliminate the unwanted lines. The last iteration performed was for a $\delta = 1$. In this step, rupture is more diffused at the back for both mat.A and mat.B and fault detection was unable to retrieve adequate fault surfaces in this location (Figure 5F).

As for the polynomial fitting, we present the results obtained for the more complex case of $\delta = 0.1$. Figure 5E2 shows that the first R^2 validation was not met. The ruptured data cloud was divided into two distinct clusters over which a secondary fitting was applied. From cluster 1, the polynomial fitting was able to extract two clear lines representing the conjugate fault system at the end of the surface slope. While, the dispersion of the data in the back of the model yielded eight different sub-clusters each represented with a given color (Figure 5E3). The ones that interest us were clusters 1.1, 1.2, 2.1 and 2.2 representing the double pop-ups.

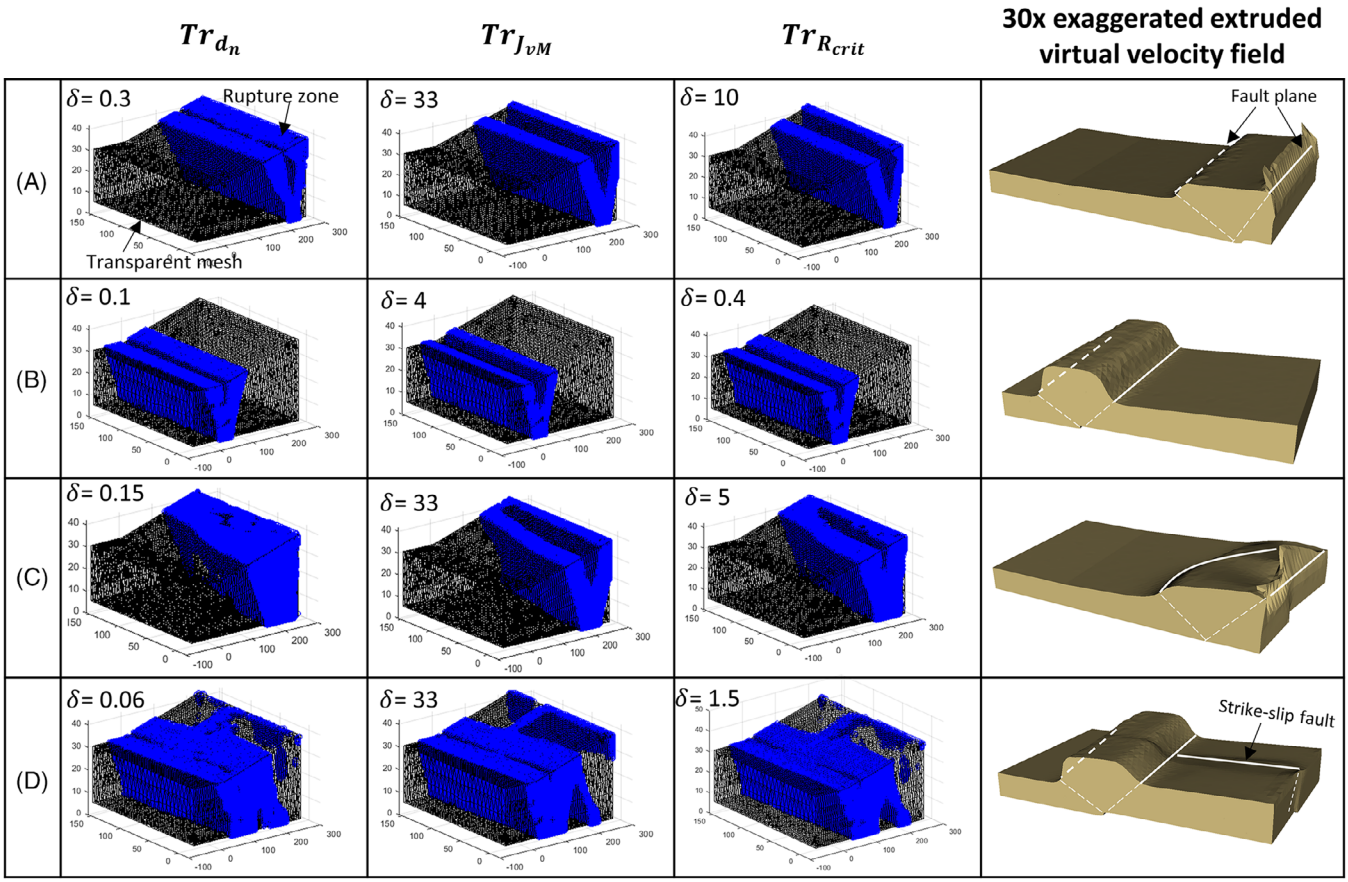

FIGURE 6 Representation of the single layer 3D model, showing the rupture zones obtained after applying the Cauchy transformations and the binarization step. Each row considers a different combination of $\phi_{\text{déc.1}}$ and $\phi_{\text{déc.2}}$ ($\phi_{\text{déc.1}} = \phi_{\text{déc.2}} = 20°$ (A), $\phi_{\text{déc.1}} = \phi_{\text{déc.2}} = 5°$ (B), $\phi_{\text{déc.1}} = 3°$ and $\phi_{\text{déc.2}} = 22°$ (C) and $\phi_{\text{déc.1}} = 10°$ and $\phi_{\text{déc.2}} = 5°$ (D)). The first column shows Tr_{d_n}, the second column $Tr_{J_{vM}}$, the third column $Tr_{R_{crit}}$ while the last column portrays a 30 times exaggerated extruded virtual velocity field. The values of the nodes verifying the rupture criteria are represented in blue and the mesh is transparent. The grid dimension is in hectometer and the vertical scale is exaggerated for a better view.

From Equation 17, The threshold values were all less than 0.65 (calculated for $\delta = 1$). For R_{crit}, these values are all considered adequate for a constrained rupture detection. Yet the higher the δ the more the rupture zones detected and the more the dispersion. To understand this tendency, we need to recall that the onset of failure is not necessarily localized onto fault planes. Initial failure may occur over wide regions, but it is only after some damaged has been accumulated and increase weakening that localization can develop on fault surfaces (e.g., ref. [39]). So the main difficulty faced in this application was not numeric but related to the wedge being in a diffuse ruptured state.

5.2 | Single layer 3D

5.2.1 | Rupture zone definition

We examine a single layer 3D model with a lateral variation of the basement friction value (Figure 1C). Figure 6 illustrates the isolated rupture zones after binarization with different values of δ, for four different combinations of $\phi_{\text{déc.1}}$ and $\phi_{\text{déc.2}}$ (the critical basement friction angle value is 8.9°).

For $\phi_{\text{déc.1}} = \phi_{\text{déc.2}} = 20°$ (A) and $\phi_{\text{déc.1}} = \phi_{\text{déc.2}} = 5°$ (B), we obtain the fundamental cases of sub-critical, or unstable, and stable wedges, respectively. In (A) for a δ value of 0.3, 33 and 10 respectively for Tr_{d_n}, $Tr_{J_{vM}}$ and $Tr_{R_{crit}}$, we obtained practically identical rupture zones with a more spread rupture zone for Tr_{d_n}. Similar results were observed for (B) under δ values of 0.1, 4 and 0.4, respectively for Tr_{d_n}, $Tr_{J_{vM}}$ and $Tr_{R_{crit}}$.

For $\phi_{\text{déc.1}} = 3°$ and $\phi_{\text{déc.2}} = 22°$ (C), the model is divided into an unstable part overlaying déc.2 and a stable part with a small sliding over déc.1. Due to the smaller lateral spread of déc.1 in comparison to déc.2, the bulk volume impacted by these décollements is not uniform. In this case, we observed that the should-be stable part of the model started sliding over déc.1 but was retained and made unstable by the unstable part which is restricted by the high friction angle of déc.2. The rupture zone obtained demonstrated a forward deviation over déc.1, with thrusting very near the back-wall over déc.2. This was confirmed by the 30-fold exaggerated extruded virtual velocity field representation. The appropriate values of δ selected were 0.15, 33 and 5 respectively for Tr_{d_n}, $Tr_{J_{vM}}$ and $Tr_{R_{crit}}$.

In the case of $\phi_{\text{déc.1}} = 10°$ and $\phi_{\text{déc.2}} = 5°$ (D), the stable part of the wedge spans over the wider décollement (déc.2) which has a value smaller than 8.9°, while the unstable wedge overlays déc.1 with a friction value higher than the critical basement value. The results obtained from this case showed a complex distribution of rupture zones. Both décollements are activated, indicating the capacity of the wedge to induce movement in the unstable portion. The failure zone is localized at the end of the surface slope, with the initiation of a strike-slip fault starting from the limit between the two décollement parts. This is also illustrated by the 30-fold exaggerated representation. In order to perform fault detection it is important to portray all aspects of this failure pattern. The smaller the δ values the more the representation focuses on the dominant faults as previously stated. By using δ values of 0.06, 33 and 1.5 respectively, for Tr_{d_n}, $Tr_{J_{vM}}$ and $Tr_{R_{crit}}$ we were able to adequately represent this failure pattern.

Finally, by closely observing both cases (A) and (B), it seems that for a weaker basement, a smaller δ value was more suited for all three criteria. In fact taking the same δ values for (B) as in (A) would have resulted in a much wider and more dispersed failure zone as was seen in Figure 2. The same observation can be done for the cases (C) and (D) presenting a heterogeneous basement. Despite it not being as evident as the previous cases, the zones overlaying décollements with higher friction angles present less dispersion in the rupture cloud and thus a thinner data concentration. This means that the optimal δ is dependent on the amount of stresses exerted over the materials. This is verified by looking at the external stress obtained at rupture (calculated from the load multiplier) for both cases (A) and (B) where the external pressure required to attain rupture in (A) was at 208 MPa while the model in (B) verified failure for a value of 119 MPa. Consequently, the less external pressure required to attain rupture the lower the δ value needed to define the ruptured zones.

5.2.2 | 2.5D fault detection approach

The aim of this section is to introduce a 2.5D extension of the previously described 2D fault detection techniques using either the Hough or Radon transforms. The proposed approach involves applying either the Hough or Radon algorithms to a set of cross-sectional slices taken at regular intervals within the same model. These lines are then combined to generate a single surface that represents the 3D fault surface. The outcomes of the transform applied to all four cases of the single layer 3D model are presented in Figure 7. We show the results obtained for 20 distinct cross-sectional slices using the Hough transform, where segmentation was already implemented, of the $Tr_{R_{crit}}$ criterion.

The results achieved for (A), (B) and (C) were promising. For (A) and (B), we were able to detect both unstable and stable failure patterns, respectively. Further, by merging the lines detected, we could accurately identify both faults and back-thrusts, as evident from the 3D and top planar views. The intersection of the detected faults with the basement allowed us to determine the curvature of these faults. Nonetheless, In case (B), near the lateral borders a small distortion was detected due to the thickness of the rupture zone. In (C), despite the heterogeneous nature of the basement, the rupture nodal cloud remained well-defined, making the application of this approach straightforward. In this instance, we anticipated a fault/back-thrust system with a curved geometry, and this was validated by the basement intersection exhibited in the top planar view. Notably, we observed some distortion near the change of décollement, which can be attributed to the difference in friction angle.

Regarding case (D), it was apparent that applying the 2.5D detection algorithm would pose a significant challenge due to the complexity of the rupture zones. We show two instances of the Hough line detection algorithm employed over diverse cross-sectional representations after interpolating the data over a 1000×100 grid and employing appropriate binarization. Observing the width of the failure zone, it becomes evident that constraining these zones with simple lines is arduous and necessitates considerable post-processing with prior knowledge of the anticipated outcome. But again we remind that in this case we deliberately considered a wider rupture zone in order to represent the full failure pattern. This is possible since we are at the onset of rupture, meaning that the model is completely near failure and complete localization over weaker surfaces has not been completed yet. In order to accommodate these large rupture areas, edge detection can be utilized as

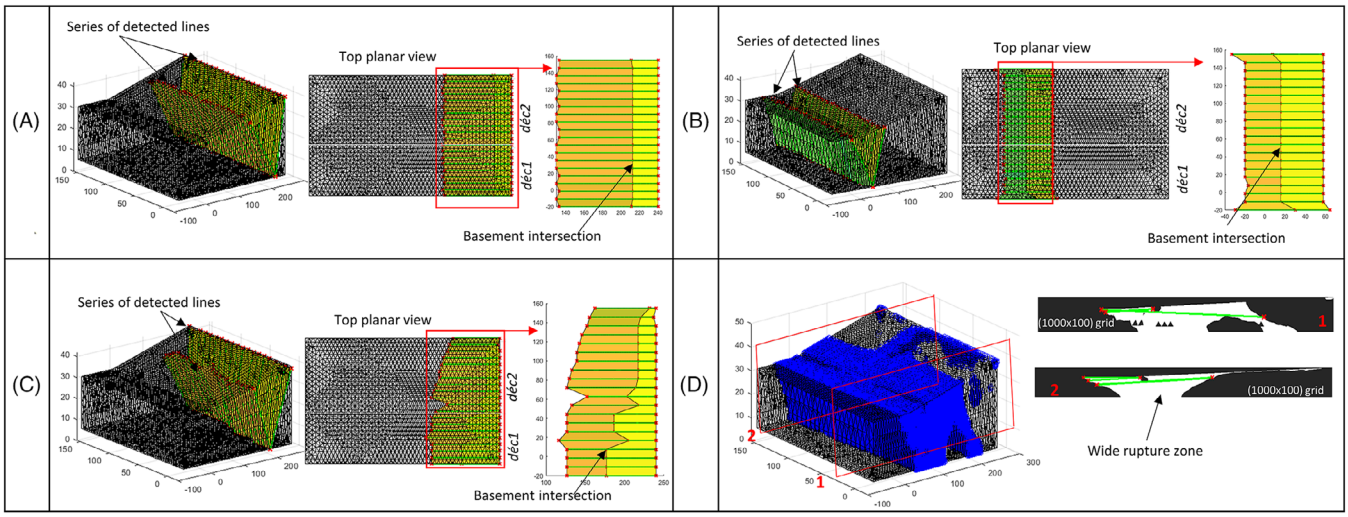

FIGURE 7 Representation of the faults detected through applying the 2.5D Hough transform approach. The four cases (A), (B), (C) and (D) represent different basement friction values (see Figure 6). The results are shown through a 3D global view of the surfaces created by joining the different lines detected. A top planar view shows the full rupture zone with the basement intersection of the faults. Case (D) shows the application of the Hough line detection over two cross-sections taken at different locations in the model, labeled 1 and 2 in red.

shown previously in the 2D multiple layer analysis. We opt for a more general approach and we decide on adopting the poly-fitting approach.

5.2.3 | 3D poly-fitting approach

We selected polynomials of degree three and followed the procedure described in Section 4.3. For (A), (B) and (C) the outcomes were satisfactory. As evident in Figure 8A-B-C, the k-means clustering managed to segregate the rupture zone between a reversed fault and a back-thrust and the fitting algorithm was able to fit each cluster with a single surface.

The complex case (D) was also investigated using the proposed algorithm. The results show that following the first R^2 check, the initial data (Figure 6D) was partitioned into three principal clusters, each represented with a different color in Figure 8D1. Each cluster was further partitioned into multiple sub-clusters, with the aim of verifying the secondary R^2 verification check. For a low secondary R^2 (lower than 50%), Figure 8D2 shows three fitted surfaces with respect to each defined cluster. These surfaces accurately show the dominant fault/back-thrust system but fail to clearly represent the failure pattern observed at the back. For the defined secondary R^2 value of 0.8, the clusters are further divided into multiple sub-clusters. Cluster 1 representing the frontal reverse fault was divided into six sub-clusters over which polynomial fitting was applied and verified the R^2 check (Figure 8D3). The same can be observed for Cluster 2 representing the back-thrust of the previously defined fault (Figure 8D4). As for Cluster 3 (Figure 8D5), it was divided into three sub-clusters each being represented by a given fitted surface. In this case, the strike-slip tendency was not detected using this method since the rupture nodes were more localized at the surface and a clear strike-slip plane has yet to be formed. Finally, we remind that in this paper, we are adopting the basic k-means clustering algorithm without prior knowledge and without additional machine learning improvements. This means that some of the discrepancies faced in extracting the faults in this case are directly related to the fact that the clustering algorithm was unable to adequately organize the diffused rupture zones.

5.3 | Multiple layer 3D

Based on the previous results, we decided to assess the effectiveness of the poly-fitting method in modeling complex geological structures. To this end, we utilized a multiple layer 3D model and set the parameters $\phi_{basement}$ to 8°, $\phi_{\text{déc.1}}$ to 15°, $\phi_{\text{déc.2}}$ to 3° and $\delta = 0.01$ for $Tr_{R_{crit}}$. Our analysis revealed that déc.2 was activated, producing a failure zone at the end of the surface slope. Although déc.1 was stimulated by the material sliding over déc.2, it remained generally inactive.

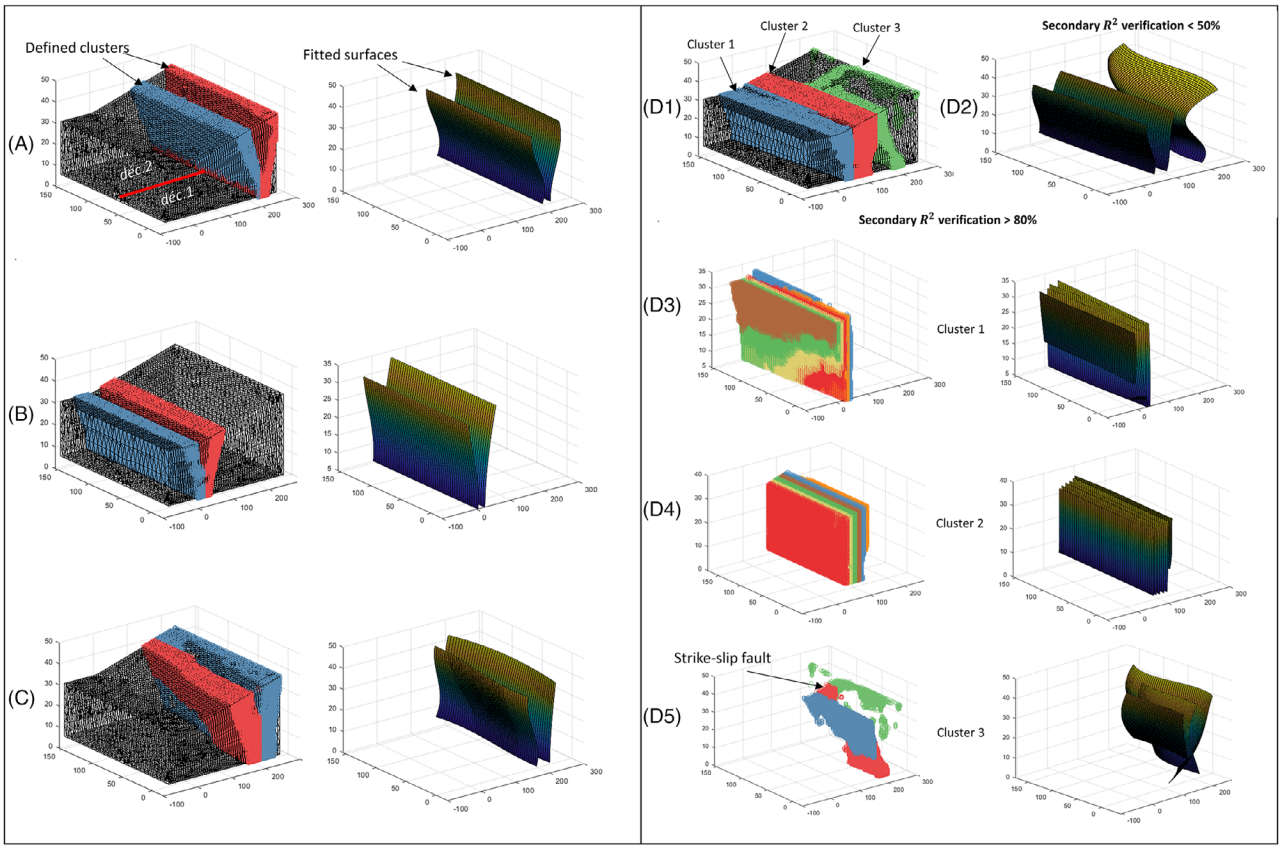

FIGURE 8 Representation of the faults detected through applying the 3D variation of the poly-fitting algorithm. The four variation of the 3D single model are represented through four different cases (A, B, C and D). The results for (A), (B) and (C) are presented by a 3D global view of the main clusters detected (in red and blue) and the surfaces fitted. For Case (D), the main clusters are shown in blue, red and green (D1), the surfaces fitted for a low secondary R^2 verification coefficient are represented in (D2) while (D3), (D4) and (D5) each show the sub clusters obtained for the three main clusters under an R^2 of 80% in addition to their respective fitted surfaces.

Moreover, the model was globally unable to slide over the defined basement, as indicated by the fault back-thrust system (Figure 9A-B) and from the 30 times exaggerated virtual velocity field (Figure 9C).

Applying the poly-fitting algorithm, the failure zone was divided into five main clusters, defining the major fault and back-thrust systems created near the back-wall and at the frontal end of the sediment layer (Figure 9D). To further refine the results, the algorithm divided these clusters into sub-clusters based on the secondary R^2 verification criterion. Consequently, a series of successive surfaces were defined to represent the identified rupture zones (Figure 9E). It is certain that by adopting a strict R^2 verification, representing a wide rupture zone yields multiple successive somewhat parallel surfaces. Nonetheless, the overall failure pattern is viably represented (Figure 9F) and the transition from the activated basement to the upper heterogeneous décollement in addition to their respective activation can also be detected through both a side and top view (Figure 9G). Finally, it goes without saying that reducing the secondary R^2 verification below 50% will result in the reduction of the number of surfaces detected as can be seen in Figure 9H, where each cluster was fitted by a single polynomial surface.

6 | DISCUSSION AND CONCLUSION

The objective of this study is to present various techniques for extracting incipient faults from a given stress field on a 2D or 3D mesh and a rupture criterion. We have established three distinct criteria based on either the stress tensor (distance d_n of the Mohr circle to the Coulomb envelope), the strain tensor (second invariant of deviatoric strain $J_{\upsilon M}$), or both ($R_{crit} = d_n/J_{\upsilon M}$). Before applying fault detection it was essential to localize rupture. For this purpose, we focused on the values of these criteria that indicate rupture using a simplified variation of the Cauchy distribution function. The scale

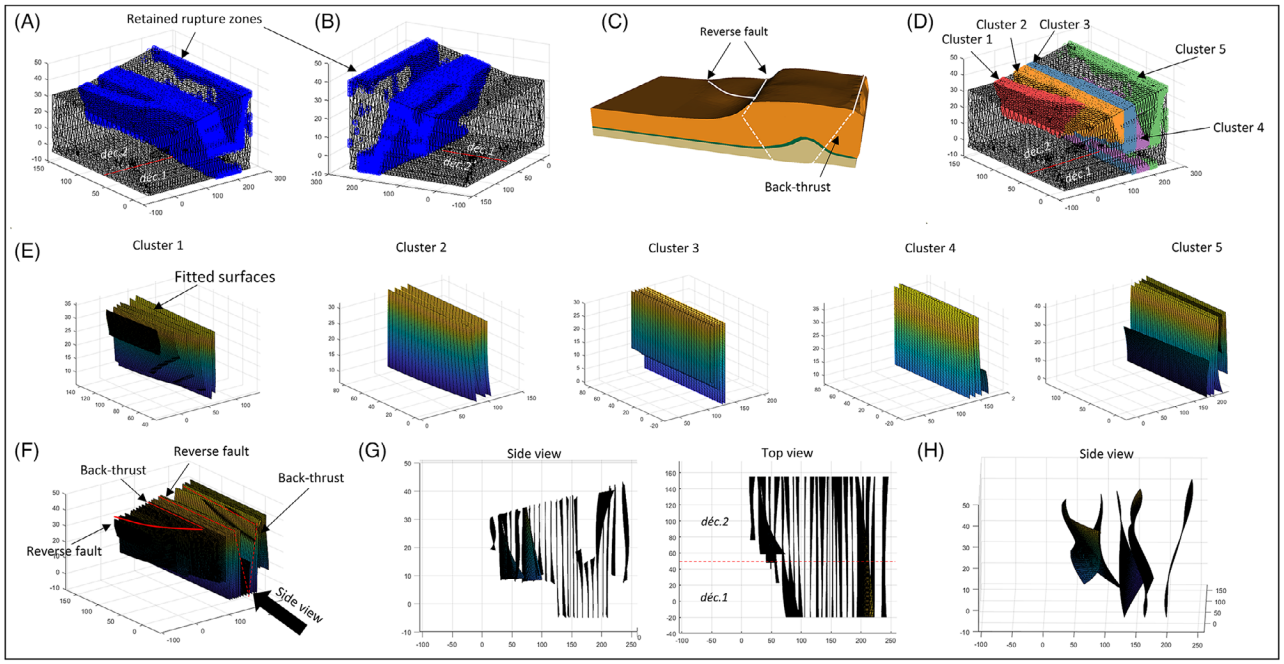

FIGURE 9 This figure shows the results obtained for the 3D multiple layer model. (A) and (B) display two representations of the ruptured data cloud from two different 3D views. The 30 times exaggerated velocity field is represented in (C), while the main clusters obtained are shown in (D). The fitted surfaces of each sub-clusters are given in (E) and the final fitted graph is portrayed in (F). The lines and dashed-lines in red explain the rupture tendency observed for each pop-up. In (G), two 2D views of the full model fitted surfaces are shown (one from the side and the other from the top). Finally in (H), the surfaces obtained through the polynomial fitting for a low secondary R^2 coefficient are shown from a side view.

parameter δ adopted in the Cauchy distribution governs the spatial distribution of the rupture zone. As for the criteria defined, d_n and R_{crit}, are the ones that verify the failure criteria and so, they can directly be used in fault detection. J_{vM} on the other hand is not a well established rupture criterion, so we simply consider that the highest deformation values are certainly occurring over the incipient faults. Although this assumption stands true for LA, since it is a rupture driven approach, the same is not valid for other types of analysis. In fact, LA is based on an independent optimization of velocity and stress fields with respect to the external load applied while accounting for the mechanical parameters of the materials. This is done at constant geometry, and the optimized external load obtained is an outcome of the calculation. On the other hand, a typical elasto-plastic calculation, for example, requires the definition of either a fixed external load or shortening, based on which it proceeds to calculate the corresponding stress and displacement fields. This means that LA and elasto-plastic calculations are of a different nature. For verification purpose, we decide to apply our approach over the single layer 2D model using an elasto-plastic finite element calculation. We conserved the same physical, mechanical and meshing parameters as in the LA example with a basement friction angle of 5°. We defined an elastic modulus at 30 GPa, a Poisson ratio of 0.25 and applied the associated flow rule. We set a shortening of 6% (to ensure reaching the plastic limit) over the rigid plate, defined at the back-wall, and we performed a long term analysis to study the model behavior over an extended period. Figure 10 shows the results obtained for all three criteria adopted using the Radon transform. The δ values chosen were 0.002, 1.3 and 0.0015 respectively for Tr_{d_n}, $Tr_{J_{vM}}$ and $Tr_{R_{crit}}$. For both Tr_{d_n} and $Tr_{R_{crit}}$, the reverse fault and back-thrust show practically the same thickness, yet for $Tr_{J_{vM}}$, the failure zone of the frontal reverse fault is thicker (Figure 10B). Nonetheless for all three criteria, we were able to extract the same fault/back-thrust system despite the small slope deviation observed in the case of $Tr_{J_{vM}}$.

The main challenge faced in this approach was the adequate choice of δ. In this paper, we used mostly LA to produce stress and strain fields, and since LA focuses on the onset of rupture, the calculation stops when at least one node fulfills the failure criterion. By closely looking at the histograms of Figure 2 we could immediately notice that the full model is in a state of failure and the majority of nodes present near zero criterion values. This was also proven by Mary et al.[39] where they showed that the onset of rupture is not necessarily localized over fault planes since at this stage, there is neither weakening nor erosion. This means that defining the rupture zone is highly dependent on the purpose of the study. For example if the aim of using this approach is to perform geological evolution, a low value of δ helps represent the dominant failure pattern. On the other hand if the aim is to detect potential failure zones in a given area, it is better to relax δ in

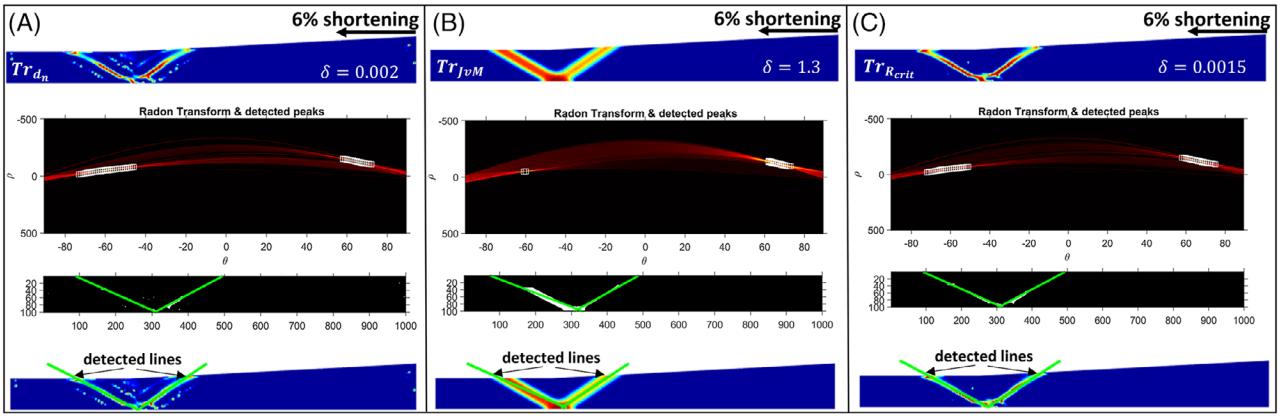

FIGURE 10 Elasto-plastic FEM calculation of the 2D single layer model subjected to 6% horizontal shortening. All three criteria were studied (Tr_{d_n} (A), $Tr_{J_{vM}}$ (B) and $Tr_{R_{crit}}$ (C)), and faults were extracted using the Radon transform. The lines detected are in green.

order to also consider the high deformation zones where rupture is imminent. In both scenarios, we must be certain not to hinder fault detection by either defining a very limited number of ruptured nodes or a significantly broad rupture zone. Following the same context, employing relatively simple structural models with homogeneous materials can also explain the lack of weak elements. In general, fractures occur and propagate through weaker portions of the material, leading to more localized rupture zones. In the present study, the homogeneity of the material can also be considered as a main reason for hindering failure convergence, resulting in a more diffuse rupture zone. This means, that the primary limitation difficulty faced in this paper is inherent to the mechanical behavior of the models more than to our method. Both material homogeneity and CCW theory explain the existence of diffused ruptured area. It is only after damage accumulation and material weakening, that failure convergence over a given surface is possible. At the onset of rupture and for homogeneous materials, these conditions are not met. In addition, based on the conducted tests and results, it was observed that δ is closely associated with the stresses applied to the model. As pressure at the back-wall increases, more nodes can be stimulated, and become more likely to attain rupture in the weaker materials. Consequently, in this case, the number of nodes that satisfy a relaxed δ is also higher.

The detection methods utilized in this study could benefit from further improvement. For instance, starting with either Hough or Radon transforms, additional image filtering techniques may be advantageous in some cases. Regarding the poly-fitting approach, despite it being more adapted for fault extraction and surface fitting in 3D, the initial clustering step is crucial. In this paper, we utilized the basic k-means clustering algorithm, which provided satisfactory results for our application. However, developing a machine learning geological application might be a better alternative since it could provide the poly-fitting method with clear examples of rupture zones and fault surfaces. In addition, we show the influence of the secondary R^2 verification criterion. For a high threshold (80%) the clusters are further divided into a series of sub-clusters each fitted into a given surface. The results obtained in this case are more accurate but somewhat excessive for simple fault extraction thus requiring post processing in order to unify the similar surfaces into a single fault. On the other hand relaxing this threshold allows for a more subtle fitting and a simpler fault surface extraction as was seen in Figure 8D2 and Figure 9H.

Finally, in numerical analysis, the slightest uncertainty in the input parameters can lead to biased results and inaccurate evaluations. In geomechanics, for example, the selection of appropriate material properties and boundary conditions has a direct impact on the deformation mechanism leading to a certain level of uncertainty in the final results obtained. This is considered quite a problem for site inspection and risk mitigation. Therefore, sensitivity analysis using numerical simulations is often considered a more reliable approach.[66–68] And thus, we hope that the presented approach helps in detecting faults through the thousands of simulations required by these sensitivity analyses.

ACKNOWLEDGMENTS

We are grateful for the Swiss Federal Nuclear Safety Inspectorate (ENSI), the Federal Office of Topography surveys Switzerland (swisstopo) and for CY Cergy-Paris University for financing the PhD scholarship of A.A.

DATA AVAILABILITY STATEMENT

The data that support the findings of this study are available from the corresponding author upon reasonable request.

ORCID

Anthony Adwan https://orcid.org/0000-0002-4902-3823

REFERENCES

1. Anderson EM. The dynamics of faulting. *Trans. Edinb. Geol. Soc.* 1905;8(3):387-402.
2. Mitcham TW. Fractures, joints, faults, and fissures. *Econ Geol*. 1963;58(7):1157-1158.
3. Wesnousky S, Scholz C, Shimazaki K, Matsuda T. Integration of geological and seismological data for the analysis of seismic hazard: a case study of japan. *Bull Seismol Soc Am*. 1984;74(2):687-708.
4. Cowie PA, Shipton ZK. Fault tip displacement gradients and process zone dimensions. *J Struct Geol*. 1998;20(8):983-997.
5. Somerville P. Seismic hazard evaluation. *BullN Z Soc Earthq Eng*. 2000;33(3):371-386.
6. John B. Chapter 2 - importance of geological studies in earthquake hazard assessment. In: Samui P, Kim D, Ghosh C, eds. *Integrating Disaster Science and Management*. Elsevier; 2018:27-40.
7. Slemmons DB, Depolo CM. Evaluation of active faulting and associated hazards. *Active Tectonics*. 1986;1986:45-62.
8. Kozłowska M, Brudzinski MR, Friberg P, Skoumal RJ, Baxter ND, Currie BS. Maturity of nearby faults influences seismic hazard from hydraulic fracturing. *Proc Natl Acad Sciences*. 2018;115(8):E1720-e1729.
9. Martin C, Kaiser P, Christiansson R. Stress, instability and design of underground excavations. *Int J Rock Mech Min Sci*. 2003;40(7):1027-1047. Special Issue of the IJRMMS: Rock Stress Estimation ISRM Suggested Methods and Associated Supporting Papers.
10. Zhang J. Borehole stability analysis accounting for anisotropies in drilling to weak bedding planes. *Int J Rock Mech Min Sci*. 2013;60:160-170.
11. Ziegler MO, Heidbach O. The 3D stress state from geomechanical–numerical modelling and its uncertainties: a case study in the Bavarian Molasse Basin. *Geothermal Energy*. 2020;8(1):1-21.
12. Augarde CE, Lee SJ, Loukidis D. Numerical modelling of large deformation problems in geotechnical engineering: a state-of-the-art review. *Soils Found*. 2021;61(6):1718-1735.
13. Hergert T, Heidbach O, Reiter K, Giger SB, Marschall P. Stress field sensitivity analysis in a sedimentary sequence of the alpine foreland, northern switzerland. *Solid Earth*. 2015;6(2):533-552.
14. Souloumiac P, Leroy Y, Maillot B, Krabbenhøft K. Predicting stress distributions in fold-and-thrust belts and accretionary wedges by optimization. *J Geophys Res Solid Earth*. 2009;114(B9).
15. Rutqvist J, Wu Y-S, Tsang C-F, Bodvarsson G. A modeling approach for analysis of coupled multiphase fluid flow, heat transfer, and deformation in fractured porous rock. *Int J Rock Mech Min Sci*. 2002;39(4):429–442. Numerical Methods in Rock Mechanics.
16. Suppe J. Fluid overpressures and strength of the sedimentary upper crust. *J Struct Geol*. 2014;69:481-492. Fluids and Structures in Fold and Thrust Belts with Recognition of the Work of David V. Wiltschko.
17. Alber M, Fritschen R, Bischoff M, Meier T. Rock mechanical investigations of seismic events in a deep longwall coal mine. *Int J Rock Mech Min Sci*. 2009;46(2):408-420.
18. Castro L, Bewick R, Carter T. An overview of numerical modelling applied to deep mining. *Innovative Numerical Modelling in Geomechanics*. CRC Press; 2012:393-414.
19. Sainoki A, Mitri HS. Dynamic behaviour of mining-induced fault slip. *Int J Rock Mech Min Sci*. 2014;66:19-29.
20. Suppe J. Geometrv and kinematics of fault-bend folding. *Am J Sci*. 1983;283:684-721.
21. Burbidge DR, Braun J. Numerical models of the evolution of accretionary wedges and fold-and-thrust belts using the distinct-element method. *Geophys J Int*. 2002;148(3):542-561.
22. Buiter SJ, Schreurs G, Albertz M, et al. Benchmarking numerical models of brittle thrust wedges. *J Struct Geol*. 2016;92:140–177.
23. McBeck JA, Cooke ML, Herbert JW, Maillot B, Souloumiac P. Work optimization predicts accretionary faulting: an integration of physical and numerical experiments. *J Geophys Res Solid Earth*. 2017;122(9):7485-7505.
24. Dieterich JH. Modeling of rock friction: 1. experimental results and constitutive equations. *J Geophys Res Solid Earth*. 1979;84(B5):2161-2168.
25. Leroy Y, Ortiz M. Finite element analysis of strain localization in frictional materials. *Int J Numer Anal Methods Geomech*. 1989;13(1):53-74.
26. Buiter SJH, Babeyko AY, Ellis S, et al. The numerical sandbox: comparison of model results for a shortening and an extension experiment. *Geol Soc London Spec Publ*. 2006;253(1):29-64.
27. Mary BC, Maillot B, Leroy YM. Predicting orogenic wedge styles as a function of analogue erosion law and material softening. *Geochem Geophys Geosyst*. 2013b;14(10):4523-4543.
28. Jing L. A review of techniques, advances and outstanding issues in numerical modelling for rock mechanics and rock engineering. *Int J Rock Mech Min Sci*. 2003;40(3):283-353.
29. Shapka-Fels T, Elmo D. Numerical modelling challenges in rock engineering with special consideration of open pit to underground mine interaction. *Geosciences*. 2022;12(5):199.
30. Castro L, Carter T, Lightfoot N. Investigating factors influencing fault-slip in seismically active structures. In: *Proceedings of the 3rd CANUS rock mechanics symposium, Toronto*, 2009:1-12.
31. Hofmann GF, Scheepers LJ. Simulating fault slip areas of mining induced seismic tremors using static boundary element numerical modelling. *Min Technol*. 2011;120(1):53-64.
32. Garcia FE, Bray JD. Distinct element simulations of earthquake fault rupture through materials of varying density. *Soils Found*. 2018a;58(4):986-1000.
33. Garcia FE, Bray JD. Distinct element simulations of shear rupture in dilatant granular media. *Int J Geomech*. 2018b;18(9):04018111.
34. Salençon J. *Théorie de la plasticité pour les applications à la mécanique des sols*. Eyrolles Paris; 1974.

35. Salençon J. *Calcul à la rupture et analyse limite*. Presses des Ponts et Chaussées, Paris; 1983:366.
36. Maillot B, Leroy Y. Kink-fold onset and development based on the maximum strength theorem. *J Mech Phys Solids*. 2006;54:2030-2059.
37. Cubas N, Leroy YM, Maillot B. Prediction of thrusting sequences in accretionary wedges. *J Geophys Res Solid Earth*. 2008;113(B12).
38. Souloumiac P, Krabbenhøft K, Leroy YM, Maillot B. Failure in accretionary wedges with the maximum strength theorem: numerical algorithm and 2D validation. *Comput Geosci*. 2010;14:793-811.
39. Mary B, Maillot B, Leroy YM. Deterministic chaos in frictional wedges revealed by convergence analysis. *Int J Numer Anal Methods Geomech*. 2013a;37(17):3036-3051.
40. Caër T, Maillot B, Souloumiac P, Frizon de Lamotte D, Nussbaum C. Mechanical validation of balanced cross-sections: the case of the Mont Terri anticline at the Jura front (NW Switzerland). *J Struct Geol*. 2015;75:32-48.
41. Dahlen FA. Critical taper model of fold-and-thrust belts and accretionary wedges. *Annu Rev Earth Planet Sci*. 1990;18(1):55-99.
42. Davis D, Suppe J, Dahlen FA. Mechanics of fold-and-thrust belts and accretionary wedges. *J Geophys Res Solid Earth*. 1983;88(B2):1153-1172.
43. Dahlen FA, Suppe J, Davis D. Mechanics of fold-and-thrust belts and accretionary wedges: cohesive coulomb theory. *J Geophys Res Solid Earth*. 1984;89(B12):10087–10101.
44. Bottero A, Negre R, Pastor J, Turgeman S. Finite element method and limit analysis theory for soil mechanics problems. *Comput Meth Appl Mech Eng*. 1980;22(1):131–149.
45. Krabbenhoft K, Lymain AV, Krabbenhoft J. OptumG2: theory. 2017. https://www.optumce.com/wp-content/uploads/2016/05/Theory.pdf
46. Zouain N, Herskovits J, Borges LA, Feijóo RA. An iterative algorithm for limit analysis with nonlinear yield functions. *Int J Solids Struct*. 1993;30(10):1397-1417.
47. Borges L, Zouain N, Huespe AE. A nonlinear optimization procedure for limit analysis. *Eur J Mech A Solids*. 1996;15:487-512.
48. Krabbenhøft K, Lyamin AV, Sloan SW. Formulation and solution of some plasticity problems as conic programs. *Int J Solids Struct*. 2007;44(5):1533-1549.
49. Jaeger J, Cook N, Zimmerman R. *Fundamentals of Rock Mechanics*. Wiley; 2007.
50. Mises Rv. Mechanik der festen körper im plastisch-deformablen zustand. *Nachrichten von der Gesellschaft der Wissenschaften zu Göttingen, Mathematisch-Physikalische Klasse*, 1913;1913:582-592.
51. Zywicz E. On the equivalence of stress- and strain-based failure criteria in elastic media. *Eur J Mech A Solids*. 1999;18(3):391-398.
52. Li X, Wu Z, Takahashi M, Yasuhara K. An experimental study on strain-based failure criteria of brittle materials. *J Appl Mech*. 2000;3:387-394.
53. Kwasniewski M, Takahashi M. Strain-based failure criteria for rocks: state of the art and recent advances. In: Zhao L, Mathier D, eds. *Rock Mech. Civ. Enviro. Eng.*, Taylor, London, 2010:45-56.
54. Tian Y, Weijermars R, Zhou F, Hu L, Liu T, Liu H. Advances in stress-strain constitutive models for rock failure: review and new dynamic constitutive failure (CDF) model using core data from the Tarim Basin (China). *Earth Sci Rev*. 2023;243:104473.
55. Hogg RV, Tanis EA, Zimmerman DL. *Probability and Statistical Inference*, Vol 993. Macmillan Publishers; 1977.
56. Sibson R. A brief description of natural neighbor interpolation. In: Barnett V, ed. *Interpreting Multivariate Data*. John Wiley & Sons; 1981:21-36.
57. Hough PV. *Method and means for recognizing complex patterns*. 1962. US Patent 3,069,654.
58. Illingworth J, Kittler J. A survey of the hough transform. *Comp Graph Image Proces*. 1988;44(1):87-116.
59. Duda RO, Hart PE. Use of the hough transformation to detect lines and curves in pictures. *Commun ACM*. 1972;15(1):11-15.
60. Borrmann D, Elseberg J, Lingemann K, Nüchter A. The 3D hough transform for plane detection in point clouds: a review and a new accumulator design. *3D Research*. 2011;2(2):1-13.
61. Radon J. On the determination of functions from their integrals along certain manifolds. *Mathematisch-Physische Klasse*, 1917;69:262-277.
62. Barrett HH. III the radon transform and its applications. *Prog Optics*, Elsevier; 1984:21;217-286.
63. MacQueen J. Classification and analysis of multivariate observations. In: *5th Berkeley Symp. Math. Statist. Probability*, 1967:281-297. University of California Los Angeles LA USA.
64. Davies DL, Bouldin DW. A cluster separation measure. *IEEE Trans Pattern Anal Mach Intell*. 1979;(2):224-227.
65. D'Errico J. polyfitn. 2023. https://www.mathworks.com/matlabcentral/fileexchange/34765-polyfitn. MATLAB Central File Exchange.
66. Iman RL, Helton JC. An investigation of uncertainty and sensitivity analysis techniques for computer models. *Risk Anal*. 1988;8(1):71-90.
67. Helton JC, Davis FJ. Illustration of sampling-based methods for uncertainty and sensitivity analysis. *Risk Anal*. 2002;22(3):591-622.
68. Saltelli A, Ratto M, Andres T, et al. *Global Sensitivity Analysis: The Primer*. John Wiley & Sons; 2008.

SUPPORTING INFORMATION

Additional supporting information can be found online in the Supporting Information section at the end of this article.

How to cite this article: Adwan A, Maillot B, Souloumiac P, Barnes C. Fault detection methods for 2D and 3D geomechanical numerical models. *Int J Numer Anal Methods*. 2024;48:607–625. https://doi.org/10.1002/nag.3652